

Strong Scatterings Invalidate Proposed Models of Enhanced TDE Rates in Post-Starburst Galaxies

ODELIA TEBOUL¹ AND HAGAI B. PERETS^{1,2}

¹*Technion – Israel Institute of Technology, Haifa, 3200002, Israel*

²*Astrophysics Research Center of the Open University (ARCO),
The Open University of Israel, P.O. Box 808, Ra’anana 4353701, Israel*

ABSTRACT

Stars wandering too close to supermassive black holes (SMBHs) can be ripped apart by the tidal forces of the black hole. Recent optical surveys have revealed that E+A galaxies are overrepresented by a factor ~ 30 , while green galaxies are overrepresented in both optical and infrared surveys. Different stellar models have been proposed to explain this Tidal Disruption Event (TDE) preference: ultra-steep stellar densities in the nuclear cluster, radial velocity anisotropies, and top-heavy Initial Mass Function (IMF). Here we explore these hypotheses in the framework of our revised loss cone theory that accounts for both weak and strong scattering, i.e., a scattering strong enough to eject a star from the nuclear cluster. We find that, when accounting for weak and strong scatterings, both ultra-steep densities and radial velocity anisotropies fail to explain the post-starburst preference of TDEs except when considering a high anisotropy factor together with a high SMBH mass and a shallow density profile of stellar mass black holes $\gamma_{\text{bh}} = 7/4$. Our findings hold when combining either model with top-heavy IMFs. Hence, new models to explain the post-starburst preference of TDEs are needed.

1. INTRODUCTION

An unlucky star wandering too close to an SMBH can be torn apart by the SMBH’s tidal forces. Roughly half of the gaseous debris from the disrupted star falls back onto the SMBH powering an extremely luminous, multi-wavelength electromagnetic flare that will typically outshine the entire host galaxy for a few months (Rees 1988). TDEs were first theoretically predicted (Hills 1975; Lacy et al. 1982; Rees 1988; Evans & Kochanek 1989) and only detected at the advent of X-ray all-sky surveys by ROSAT only later, with the advent of X-ray all-sky surveys by ROSAT (Bade et al. 1996).

The sample of observed TDEs has been growing at an increasing rate and now spans all wavelengths, from the radio to gamma-rays. Optical surveys revealed a surprising over-representation of these events in post-starburst galaxies (Arcavi et al. 2014; French et al. 2016, 2017; Law-Smith et al. 2017; Graur et al. 2018; French et al. 2020; Hammerstein et al. 2021). This overrepresentation was initially estimated to be $\sim 100 - 190$ in E+A galaxies, galaxies that makeup $\sim 0.2\%$ of low-redshift galaxies, and whose recent starburst created $> 3\%$ of

their current stellar mass over 25–200 Myr (French et al. 2016). Quiescent Balmer-strong galaxies which make up $\sim 2\%$ of local galaxies, and which formed $> 0.1\%$ of their current stellar mass over 25 Myr – 1 Gyr exhibited a smaller boost of ~ 30 (French et al. 2016). Law-Smith et al. (2017) showed that accounting for selection effects could reduce the TDE boost in E+A galaxies to a factor $\sim 25 - 48$, while the latest estimations suggest that E+A galaxies are overrepresented by a factor of $\sim 22 - 29$ (Hammerstein et al. 2021). A less significant preference for green valley galaxies was also observed in optical surveys (Hammerstein et al. 2022; Yao et al. 2023) as well as in Infrared (IR) survey (Masterson et al. 2024).

Several hypotheses have been proposed to explain this puzzling preference for post-starburst galaxies. Assuming that post-starburst galaxies stem from galaxy mergers, Arcavi et al. (2014) proposed that the post-starburst preference could be triggered by SMBH binaries. Madi-gan et al. (2018) found that an eccentric nuclear disk could significantly enhance TDE rates and hence explain the preference if eccentric nuclear disks form during galaxy mergers. The presence of an AGN disk was also found to increase TDE rates by a factor of ~ 10 (e.g., Kennedy et al. (2016); Kaur & Stone (2024); however Wang et al. (2024) found larger enhancements). The interaction of stars with massive perturbers and/or nuclear spiral arms could also slightly increase TDE rates,

by up to a factor of two (Perets et al. 2007a; Hamers & Perets 2017).

Other proposed explanations invoke Nuclear Star Cluster (NSC) star characteristics: ultra-steep stellar densities with $\rho \propto r^{-\gamma_*}$, $\gamma_* \geq 9/4$ (Stone et al. 2018), radial velocity anisotropies (Stone et al. 2018) and a complete stellar function with a top-heavy IMF (Bortolas 2022). Both ultra-steep stellar densities and radial velocity anisotropies were found to increase TDE rates by factors up to a few hundreds.

In addition to this puzzling post-starburst preference, optical surveys observed TDE rates were constrained to a range $\dot{N}_{\text{TDE}} \sim 10^{-5} - 10^{-4} \text{ yr}^{-1} \text{ gal}^{-1}$ (Holoien et al. 2016; van Velzen 2018; Yao et al. 2023). However, theoretically predicted rates computed with classical loss cone theory were typically estimated in the range $\dot{N} \sim 10^{-4} - 10^{-3} \text{ yr}^{-1} \text{ gal}^{-1}$ (e.g., Wang & Merritt (2004); Stone & Metzger (2016)). This discrepancy between observed and theoretically predicted rates worsens in non-E+A galaxies, as the post-starburst preference of TDEs observed in several surveys further reduces the observed rates in non-E+A galaxies.

Classical loss cone theory calculations are carried out by resolving the Fokker-Planck equation that focuses on the cumulative effect of many weak scatterings. Strong or small impact parameter scatterings are generally neglected, as they are largely outnumbered by weak scatterings. However, most stars that become TDEs come from within the radius of influence, *the densest environments of the Universe*. In such environments, close encounters rare elsewhere can become non-negligible.

Hence, we proposed a revised loss cone theory taking into account both weak interactions and other close encounters: strong scattering, tidal captures, and direct collisions (Teboul et al. (2024), hereafter TSO24). We found that, at the radius of influence, the dominant mechanism is strong scattering, i.e. a scattering strong enough to eject the test star from the distribution. We showed that, depending on the black hole density slope γ_{bh} , *TDE rates are reduced by up to an order of magnitude*, reconciling them with observed TDE rates (e.g. Yao et al. (2023)).

The black hole density slope depends on the segregation mode. Indeed, in a system composed of both stars and heavier objects, the heavier objects are expected to segregate towards the center of the galactic nucleus and settle on a steeper cusp while the light objects will have a weaker cusp $\gamma_* \approx 1.3 - 1.5$. In the weak segregation limit, the black hole slope assumes $\gamma_{\text{bh}} = 7/4 - 2$ (Bahcall & Wolf 1977; Preto & Amaro-Seoane 2010; Amaro-Seoane & Preto 2011; Broggi et al. 2022) whereas in the strong segregation limit, the heavy

objects have been predicted to settle to even steeper power-law slopes of $\gamma_{\text{bh}} = 2 - 11/4$ (Alexander & Hopman (2009); see also Zhang & Amaro Seoane (2024); Aharon & Perets (2016)).

Here we investigate the proposed explanations invoking NSC star characteristics for the post-starburst preference of TDEs in the framework of our revised loss cone theory that takes into account both weak and strong scattering.

We present classical loss cone theory in Section 2, briefly summarize the key results of strong scattering in Section 2.1, and present our modified Fokker-Planck equation with strong scattering in Section 2.2. In Section 3 we explore the effect of radial velocity anisotropies with and without strong scattering, while in Section 4 we investigate the impact of ultra-steep stellar densities. In Section 5, we combine the effect of different Present Day Mass Function (PDMF) with radial velocity anisotropies and then ultra-steep densities. In Section 6, we discuss enhancements obtained with other proposed scenarios and summarize our results in Section 7.

2. LOSS CONE THEORY

2.1. Classical loss cone theory

In NSC, stars and compact objects evolve over time due to two-body relaxation. In a spherical galaxy, the distribution function of stars $f(\mathbf{x}, \mathbf{v})$ can be transformed by Jeans' theorem to $f(\epsilon, J)$, where ϵ and J are the specific energy and angular momentum of a stellar orbit. Although stars diffuse in both energy ϵ and angular momentum J , for the near-radial orbits relevant for TDEs, the dominant and more rapid mechanism is the diffusion in angular momentum and we can write $f(\epsilon, J) = f_\epsilon(\epsilon)f_j(J)$. Assuming a frozen distribution of energy, stars are fixed in bins of orbital energy but are allowed to diffuse through angular momentum space through a random walk evolution. This process can be captured by the orbit-averaged Fokker-Planck equation (e.g. Bahcall & Wolf (1976); Magorrian & Tremaine (1999)):

$$\frac{\partial f}{\partial \tau} = \frac{1}{4j} \frac{\partial}{\partial j} \left(j \frac{\partial f}{\partial j} \right) \quad (1)$$

where $j \equiv J/J_c(\epsilon) = \mathcal{R}^{1/2}$ is a dimensionless angular momentum variable (normalized by the angular momentum of a circular orbit, J_c), $\tau \equiv \mu(\epsilon)t \approx t/t_\tau$ is a dimensionless time variable (normalized by the energy relaxation time t_r) and $\mu(\epsilon)$ the orbit-averaged diffusion coefficient at specific energy ϵ :

$$\mu(\epsilon) = \frac{1}{P(\epsilon)} \oint \frac{dr}{v_r} \lim_{\mathcal{R} \rightarrow 0} \frac{\langle (\Delta \mathcal{R})^2 \rangle}{2\mathcal{R}}. \quad (2)$$

Here $P(\epsilon)$ is the orbital period of a radial orbit of energy ϵ , v_r is the star's radial velocity, and the local diffusion coefficient $\langle(\Delta\mathcal{R})^2\rangle$ is presented in Appendix A.

The stellar distribution function $f_\star(\epsilon)$ is calculated using Eddington's formula which can be simplified to:

$$f_\star(\epsilon) = 8^{-1/2} \pi^{-3/2} \frac{\Gamma(\gamma_\star + 1)}{\Gamma(\gamma_\star - 1/2)} \frac{\rho_{\text{infl}}}{\langle m_\star \rangle} \left(\frac{GM_\bullet}{r_{\text{infl}}} \right)^{-\gamma_\star} \epsilon^{\gamma_\star - 3/2} \quad (3)$$

for an isotropic stellar distribution with a density profile $\rho(r) = \rho_{\text{infl}}(r/r_{\text{infl}})^{-\gamma_\star}$ and a Keplerian potential $\psi = GM_\bullet/r$. The (positive-definite) specific orbital energy is, for a given star at radius r and velocity v , $\epsilon = \psi(r) - v^2/2$; $\langle m_\star \rangle$ is the average mass in the stellar population; and the radius of influence r_{infl} is defined as the radius that encloses a total mass of stars equal to the SMBH mass.

2.2. Impact of strong scattering

In addition to their numerous weak encounters, stars also have a much smaller number of strong encounters that are not taken into account in the classical Fokker-Planck equation. Those strong encounters are much less numerous than weak encounters but, as we have shown in TSO24, they are efficient at removing stars on highly eccentric orbits, i.e., the stars that could have become TDEs. Let us briefly summarize the conditions for a star to be ejected. Let us consider a test star whose velocity is \mathbf{V} while its velocity after a strong encounter becomes $\mathbf{V} + \delta\mathbf{v}$. Let θ be the angle between \mathbf{V} and $\delta\mathbf{v}$, with v_{esc} the escape velocity at this point. The star will be ejected if (Hénon 1960):

$$V^2 + \delta v^2 + 2V\delta v \cos\theta \geq v_{\text{esc}}^2. \quad (4)$$

This condition for ejection (Eq. 4) remains the same for both strong encounters with equal mass scatterers and unequal mass scatterers.

Assuming Keplerian motion and an escape velocity $v_{\text{esc}} = \sqrt{2GM_\bullet/r}$, for equal mass scatterers, the local ejection rate writes, (TSO24):

$$\dot{N}_{\text{ej}} = \frac{2^{2-\gamma_\star} \pi \rho_{\text{infl}} a^2 m_\star V^{1+2\gamma_\star}}{(1+\gamma_\star)M^2} \left(\frac{GM_\bullet}{r_{\text{infl}}} \right)^{-\gamma_\star} \quad (5)$$

with V the local Keplerian velocity of the test star and a its semimajor axis.

Whereas for unequal mass scatterers, the local ejection rate becomes, (TSO24):

$$\dot{N}_{\text{ej,u}} = 16\pi^2 G^2 m_{\text{bh}}^2 \left(\int_{v_1}^{v_2} I_A f_{\text{bh}}(v) v dv + \int_{v_2}^{v_3} I_B f_{\text{bh}}(v) v dv + \int_{v_3}^{v_{\text{esc}}} I_C f_{\text{bh}}(v) v dv \right) \quad (6)$$

where

$$\begin{aligned} I_A &= \frac{2 [v^2 - \alpha (v_{\text{esc}}^2 - V^2)]^{3/2}}{3V (v_{\text{esc}}^2 - V^2)^2} \\ I_B &= \frac{2 [v^2 - \alpha (v_{\text{esc}}^2 - V^2)]^{3/2} + v [2v^2 - 3\alpha (v_{\text{esc}}^2 - V^2)]}{6V (v_{\text{esc}}^2 - V^2)^2} \\ &\quad - \frac{(2v_{\text{esc}} + V)}{6V (v_{\text{esc}} + V)^2} + \frac{(1+\alpha)^2}{8V (V+v)} \\ I_C &= \frac{3v_{\text{esc}}^2 - V^2}{3 (v_{\text{esc}}^2 - V^2)^2} + \frac{(1+\alpha)^2}{4 (V^2 - v^2)} \end{aligned} \quad (7)$$

and the integration limits are given by:

$$\begin{aligned} v_1 &= \sqrt{\alpha (v_{\text{esc}}^2 - V^2)} \\ v_2 &= \frac{1}{2} [(1+\alpha)v_{\text{esc}} - (1-\alpha)V] \\ v_3 &= \frac{1}{2} [(1+\alpha)v_{\text{esc}} + (1-\alpha)V] \end{aligned} \quad (8)$$

As the orbital period is short compared to the relaxation time, local ejection rates per star can then be orbit averaged. The closed forms that we derived in TSO24 for some physically motivated values of γ_{bh} can be found in Appendix B.

2.3. Modified Fokker-Planck equation

As we have shown, the ejection of stars from the distribution due to strong scatterings can be modeled by adding a sink term to the Fokker-Planck equation, which becomes (TSO24):

$$\frac{\partial f}{\partial \tau} = \frac{1}{4j} \frac{\partial}{\partial j} \left(j \frac{\partial f}{\partial j} \right) - \frac{\langle \dot{N}_{\text{ej}} \rangle}{\mu(\epsilon)} f. \quad (9)$$

where $\langle \dot{N}_{\text{ej}} \rangle$ is the orbit-averaged rate of ejection due to strong scattering, j and τ are dimensionless angular momentum and times as defined in the previous section.

The initial and inner boundary conditions depend on a dimensionless diffusivity parameter $q(\epsilon) = \mu(\epsilon)P(\epsilon)/j_{\text{lc}}^2(\epsilon)$, which determines whether the loss cone evolves in the “empty” ($q \ll 1$; stars immediately destroyed once $j \leq j_{\text{lc}}$) or “full” ($q \gg 1$; stars may move in and out of the loss cone multiple times per orbit) limits.

For an empty loss cone an absorbing boundary condition at the loss cone can be assumed while for a full loss cone, the distribution function only goes to zero at a much smaller value of dimensionless angular momentum, $j_0 = j_{\text{lc}}(\epsilon) \exp(-\alpha/2)$, where

$$\alpha(q) \approx (q^2 + q^4)^{1/4} \quad (10)$$

is an approximate flux variable that smoothly bridges the empty and full loss cone limits (Cohn & Kulsrud 1978; Merritt 2013). The presence of a sink term does not impact α as long as $j_o \ll j_{lc}$ (TSO24). Hence the boundary conditions are:

$$f(j \leq j_0, t) = 0; \quad \left. \frac{\partial f}{\partial j} \right|_{j=1} = 0. \quad (11)$$

The flux of stars that scatter into the loss cone per unit of time and energy is given by:

$$\mathcal{F}(t; \epsilon) = 2\pi^2 \mu(\epsilon) P(\epsilon) J_c^2(\epsilon) f_\epsilon(\epsilon) \left(j \frac{\partial f_j(j, t)}{\partial j} \right)_{j=j_{lc}}. \quad (12)$$

Then, time-dependent TDE rates are obtained by integrating $\mathcal{F}(\epsilon)$ across many bins of energy ϵ , such that:

$$\dot{N}_{\text{TDE}}(t) = \int \mathcal{F}(t; \epsilon) d\epsilon. \quad (13)$$

We derived analytical solutions of the modified Fokker-Planck equation with strong scattering Eq. 9 using the method of Frobenius (TSO24). The analytical solutions for different slopes of scatterers can be found in Appendix C.

3. RADIAL VELOCITY ANISOTROPIES

Velocity anisotropies i.e., the extent to which stellar orbits are predominantly radial or tangential have an influence on the number of stars getting tidally disrupted. Indeed, only stars with high eccentricities (low normalized angular momentum $j \leq j_{lc}$) can become TDEs. Hence, anisotropic distributions with more (respectively less) eccentric stars than the isotropic distribution would give rise to a higher (respectively lower) number of disrupted stars. Lezhnin & Vasiliev (2015) explored the impact of an anisotropic distribution with more tangential velocities and found that it could reduce the number of TDEs for a fraction of the relaxation time. Stone et al. (2018) proposed that the infall and tidal disruption of young massive clusters could give rise to an opposite distribution harboring a preference towards the radial component and found that, depending on the bias, TDE rates could be enhanced by a factor up to a few hundreds for up to the relaxation time.

Here, we explore the impact of such radial velocity anisotropies on TDE rate in the framework of our revised loss cone theory that takes into account both weak and strong scattering (TSO24). The anisotropy parameter β_a characterizing the extent to which stellar orbits are predominantly radial or tangential can be parametrized as:

$$\beta_a \equiv 1 - \frac{T_\perp}{2T_\parallel} \quad (14)$$

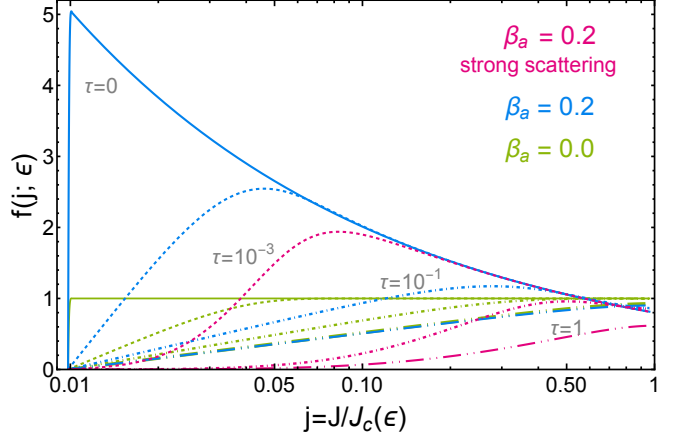


Figure 1. Evolution of the distribution function $f(j; \epsilon)$ as a function of the dimensionless angular momentum j at fixed energy ϵ , shown for different snapshots in dimensionless time $\tau = 0$ (solid), $\tau = 10^{-3}$ (dashed), $\tau = 10^{-1}$ (dot-dashed) and $\tau = 1$ (dot-dot-dashed). Green lines correspond to an isotropic stellar cluster ($\beta_a = 0$). Blue lines show a case with moderate initial radial anisotropy ($\beta_a = 0.2$) without strong scatterings while pink lines show the same case with strong scatterings. All curves are shown in the empty loss cone regime with $q = 0.006$ for a SMBH with $M_\bullet = 10^{6.5} M_\odot$ and stars with a power law density $\gamma_\star = 3/2$.

where T_\perp and T_\parallel are the kinetic energies of tangential and radial motion respectively, with $\beta_a = 1$ corresponding to all orbits being radial and $\beta_a = 0$ to an isotropic distribution. Hence, the initial condition for anisotropic velocity distributions writes: ¹

$$f_j(j, t = 0) = \frac{1 - \beta_a}{1 - j_{lc}^{2-2\beta_a}} j^{-2\beta_a}, \quad j_{lc} < j \leq 1 \quad (15)$$

Fig.1 showcases the evolution of the distribution function at different times for a radially-biased distribution with $\beta_a \sim 0.2$ with and without strong scattering as well as the evolution with an isotropic distribution.

Without strong scattering, the change induced by the anisotropic distribution washes out after a relaxation time t_r (i.e., $\tau = 1$). However, when taking into account both weak and strong scattering, higher eccentricities stars (i.e., $j \leq 0.03$) are more depleted than the isotropic distribution at early times $\tau \sim 10^{-3} t_r \sim 10^6$ years. At later times $\tau \sim 0.1 t_r$, stars with all angular momentum are more depleted than in the case with an isotropic distribution. As we have shown in (Teboul et al. 2024), strong scatterings are more efficient at depleting stars with the most radial orbits i.e. lower angular momentum. Hence, an anisotropic distribution with more stars

¹ The condition is identical to the condition considered in Stone et al. (2018)

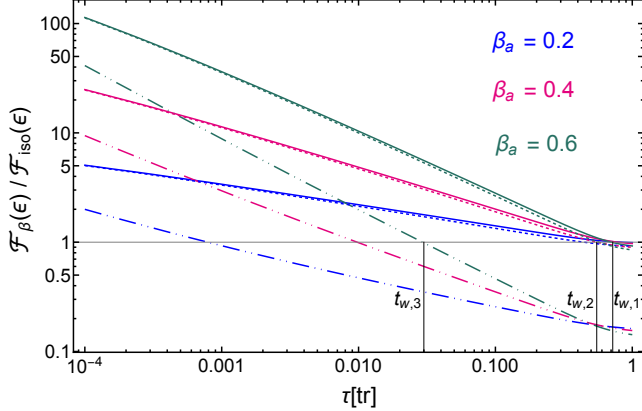


Figure 2. Time evolution of the flux of stars into the SMBH loss cone (\mathcal{F}_β) normalized to the equivalent stellar flux for isotropic initial conditions, (\mathcal{F}_{iso}) for a SMBH with $M_\bullet = 10^{6.5} M_\odot$ and a density power law of stars $\gamma_\star = 3/2$. The horizontal axis is normalized to the relaxation time t_r . We consider three different anisotropy factors: $\beta_a = 0.2$ (blue), $\beta_a = 0.4$ (pink) and $\beta_a = 0.6$ (green). The full lines show the flux enhancements without strong scattering, the dashed lines depict the case of strong scattering $\gamma_{\text{bh}} = 7/4$, and the dot-dashed lines show the case of strong scattering and $\gamma_{\text{bh}} = 5/2$. The maximum times for the enhancements to completely wash out are also indicated: $t_{w,1}$ (without strong scatterings), $t_{w,2}$ (strong scatterings: $\gamma_{\text{bh}} = 7/4$), $t_{w,3}$ (strong scatterings: $\gamma_{\text{bh}} = 5/2$).

with lower angular momentum induces a short-lived enhancement then followed by a stronger depletion of stars compared to the isotropic distribution.

This effect is further explored in Fig.2 which presents the flux of stars into the loss cone for an anisotropic distribution normalized by the isotropic flux of stars where fluxes are obtained with Eq.12. As expected, higher anisotropic factors give rise to higher enhancements. Without strong scatterings, depending on the anisotropy parameter β_a , fluxes are enhanced by a factor 5 – 100. For all anisotropy parameters β_a , those enhancements wash out at $t_{w,1} \approx 0.7 t_r$. However, with strong scattering, enhancements and duration of those enhancements t_w strongly depend on the stellar mass black hole density slope γ_{bh} . In the case of weak segregation: $\gamma_{\text{bh}} = 7/4$, the evolution of the enhancements induced by the different anisotropy factors is very similar to the evolution without strong scattering albeit the time for the enhancements to wash out is slightly smaller $t_{w,2} \approx 0.5 t_r$. For strong segregation and $\gamma_{\text{bh}} = 5/2$, the fluxes are only enhanced by a factor 2 – 40 at most and wash out early on at $t_{w,3} \approx 10^{-3} - 10^{-2} t_r$, depending on the anisotropy factor. It is important to note, that *enhancements turn into reduction for most of the relaxation time when accounting for strong scatterings.*

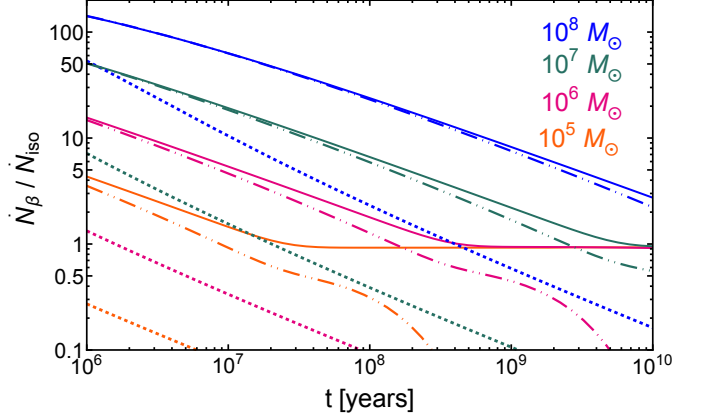


Figure 3. Evolution of TDE rate enhancements: $\dot{N}_\beta / \dot{N}_{\text{iso}}$ for an anisotropy factor $\beta_a = 0.5$ as a function of post-starburst time t . Different colors correspond to different SMBHs as labeled in the figure. The full lines show the rate enhancements without strong scattering, the dashed lines depict the case of strong scattering and $\gamma_{\text{bh}} = 7/4$, and the dot-dashed lines show the case of strong scattering and $\gamma_{\text{bh}} = 5/2$.

The fluxes of stars inside the loss cone are then integrated over a large number of energy bins following Eq.13. Fig.3 showcases the evolution of TDE rate enhancements: $\dot{N}_\beta / \dot{N}_{\text{iso}}$ for an anisotropy factor $\beta_a = 0.5$, chosen to be constant across all orbital energies ϵ and close to the maximum anisotropy factor, guaranteeing stability (e.g. Merritt & Aguilar (1985)).

Without strong scattering, the enhancements induced by the anisotropic distribution depend on the SMBH mass: ranging from 4 for a $M_\bullet = 10^5 M_\odot$ to 150 for a $M_\bullet = 10^8 M_\odot$. The enhancements diminish with time such as $\dot{N}_{\beta_a} / \dot{N}_{\text{iso}} \propto t^{-\beta_a}$ until reaching a plateau at t_w , the time for enhancements to wash out. As shown in Fig. 2, t_w is a fraction of the relaxation time and hence increases with the mass of the SMBH.

With strong scattering, the evolution depends on the power-law density slopes of stellar mass black holes γ_{bh} . For $\gamma_{\text{bh}} = 7/4$, the evolution is similar to the one without strong scattering for higher SMBH masses. For smaller SMBH masses, the time for enhancements to wash out t_w is small enough that enhancements turn into reductions after $\sim 10^7$ Myr for $M_\bullet = 10^5 M_\odot$ and $\sim 10^8$ Myr for $M_\bullet = 10^6 M_\odot$. However for $\gamma_{\text{bh}} = 5/2$, strong scatterings are so efficient that, even after 1 Myr, the enhancements induced by the anisotropic distribution have already washed out for $M_\bullet \leq 10^6 M_\odot$ and are a factor 50 for a $M_\bullet = 10^8 M_\odot$. It can also be noted that enhancements diminish at a slightly higher rate and hence after 20 Myr, *enhancements have turned into reductions* for SMBH up to $M_\bullet = 10^7 M_\odot$ and are a mere factor 6 for $M_\bullet = 10^8 M_\odot$.

4. ULTRA-STEEP STELLAR DENSITIES

In a relaxed nuclear star cluster (NSC), stars are expected to settle to the well-known Bahcall–Wolf cusp $\gamma_\star = 7/4$ in the absence of heavier objects while a weaker cusp $\gamma_\star \approx 1.3 - 1.5$ is expected in their presence (e.g., Bahcall & Wolf (1976, 1977)). Ultra-steep profile with $\gamma_\star \approx 2.25 - 2.5$ could be formed in the case of a very centrally concentrated (i.e. inside the sphere of influence) star formation (Generozov et al. 2018). Moreover, Young (1980) showed that the stellar slope may assume steeper values of $\gamma_\star \gtrsim 2$, for an adiabatically growing SMBH.

Stone et al. (2018) found that ultra-steep density profiles with $\gamma_\star \approx 2.25 - 2.5$ could enhance TDE rates by a factor $\approx 10 - 100$. As we showed that the efficiency of strong scattering highly depends on the density slopes of the scatterers, we explored the effect of ultra-steep density profiles of stars considering the effect of strong scattering at early times when the erosion of the cusp was negligible (TSO24). We found that strong scattering could reduce the enhancements induced by ultra-steep densities (Fig. 10, TSO24). Motivated by these findings, we further explore this effect here considering the effect of strong scattering from both stars and stellar mass black holes. We also account for the erosion of the cusp and hence can compute the evolution with time of ultra-steep stellar densities with strong scatterings.

Assuming a stellar density slope γ_\star , stellar-mass black holes stemming from such a distribution of stars will acquire a density slope γ_{bh} such that $\gamma_{\text{bh}} \geq \gamma_\star$. Hereafter, to be conservative, we shall assume that $\gamma_{\text{bh}} = \gamma_\star$. Ultra-steep stellar density profiles will result in much shorter relaxation times, especially at small energies. An ultra-steep cusp erodes from the inside out and the ultra-steep density evolves from a power law $\rho \propto r^{-\gamma_{\text{steep}}}$ to a broken power law:

$$\rho(r, t) = \begin{cases} \rho_{\text{infl}}(r/r_{\text{infl}})^{-\gamma_{\text{steep}}}, & r > r_{\text{b}}(t) \\ \rho_{\text{infl}}(r/r_{\text{b}}(t))^{-\gamma_{\text{rel}}}(r_{\text{b}}(t)/r_{\text{infl}})^{-\gamma_{\text{steep}}}, & r \leq r_{\text{b}}(t) \end{cases} \quad (16)$$

where γ_{steep} is the initial ultra-steep value of the cusp while γ_{rel} is the relaxed value, r_{b}, is . We compute the evolution of the density slopes of the stellar mass black holes $\gamma_{\text{bh}}(t)$ and stars $\gamma_\star(t)$ by solving the one-dimensional time-dependent Fokker-Plank equation in energy with the code PHASEFLOW developed by Vasiliev (2017).

Fig. 4 shows the evolution of the densities slopes $\gamma_\star(t)$ and $\gamma_{\text{bh}}(t)$ at different times for a SMBH $M_\bullet = 10^{6.5} M_\odot$ for an initial ultra-steep profile $\gamma_\star = \gamma_{\text{bh}} = 5/2$. After the erosion, the power law density becomes a broken

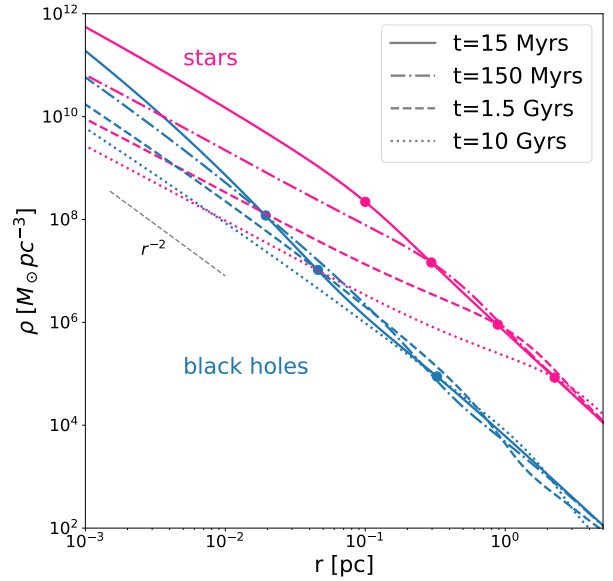


Figure 4. Evolution of an initially ultrasteep profile of stars and stellar mass black holes: $\rho \propto r^{-\gamma}$, $\gamma_\star = \gamma_{\text{bh}} = 5/2$ using the PHASEFLOW code. Here we consider a SMBH with mass $M = 10^{6.5} M_\odot$. Pink lines showcase the evolution of stars while blue lines correspond to stellar-mass black holes. The different lines correspond to post-starburst ages $t = 15$ Myrs (solid), $t = 150$ Myrs (dot-dashed), $t = 1.5$ Gyrs (dotted) and $t = 10$ Gyrs (dotted). The dots mark the break radius r_{b} at different times for both star and stellar mass black holes.

power law as defined in Eq. 16. The break radius for both stars and stellar-mass black holes are indicated by the dots for different times. The stellar-mass black holes erode more slowly than the stars: at $t = 15$ Myr, $r_{\text{b},\star} \sim 10^{-1}$ parsecs while $r_{\text{b},\text{bh}} < 10^{-3}$ parsecs.

Considering a broken power-law density has implications at different steps of the calculation. Firstly, for such a broken power-law, making use of the Eddington’s formula the density function becomes:

$$f(\epsilon, t) = 8^{-1/2} \pi^{-3/2} \frac{\Gamma(\gamma_{\text{rel}} + 1)}{\Gamma(\gamma_{\text{rel}} - 1/2)} \frac{\rho_{\text{infl}}}{\langle m_\star \rangle} \left(\frac{GM_\bullet}{r_{\text{b}}(t)} \right)^{-\gamma_{\text{rel}}} \times \left(\frac{r_{\text{b}}(t)}{r_{\text{infl}}} \right)^{-\gamma_{\text{steep}}} \epsilon^{\gamma_{\text{rel}} - 3/2} \quad (17)$$

This change on the density function impacts the orbit-averaged diffusion coefficient $\mu(\epsilon)$ which becomes time-dependent: $\mu(\epsilon, t) \propto r_{\text{b},\star}(t)^{-\gamma_{\text{steep},\star} + \gamma_{\text{rel},\star}}$.

Local ejection rates for strong scattering are also modified when taking into account a broken power-law and become time-dependent. For equal mass scatterers, we

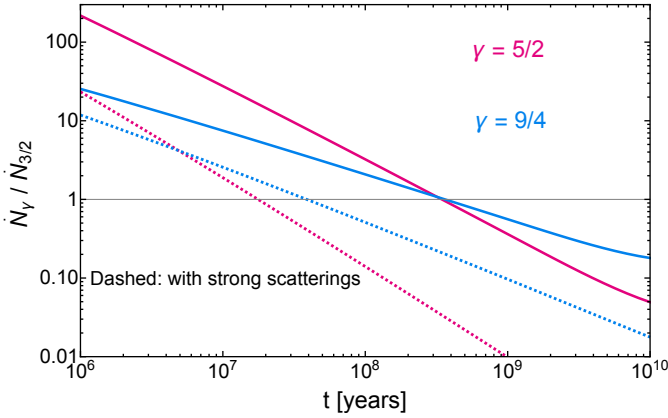


Figure 5. Evolution of TDE Rate enhancements: $\dot{N}_\gamma/\dot{N}_{3/2}$ for a SMBH $M_\bullet = 10^{6.5}M_\odot$ as a function of post-starburst time t . Blue lines correspond to an initial ultra-steep profile of both stars and black holes of $\gamma = 9/4$ while pink lines correspond to $\gamma = 5/2$. The full lines show the rate enhancements without strong scattering while dashed lines show the evolution with strong scattering. The densities of both stars and stellar mass black holes have been evolved with the code Phaseflow, see Fig. 4.

find that the local ejection rate becomes:

$$\dot{N}_{\text{ej}}(t) = \frac{2^{2-\gamma_{\text{rel}}}\pi\rho_{\text{infl}}a^2m_\star V^{1+2\gamma_{\text{rel}}}}{(1+\gamma_{\text{rel}})M^2} \times \left(\frac{GM_\bullet}{r_b(t)}\right)^{-\gamma_{\text{rel}}} \left(\frac{r_b(t)}{r_{\text{infl}}}\right)^{-\gamma_{\text{steep}}} \quad (18)$$

Interestingly, the average ejection rate for equal mass scatterer has the same time dependence as the orbit-averaged diffusion coefficient μ . Hence, the sink term for equal mass scatterers does not depend on time. However, for unequal mass scatterers, the unequal ejection rate has the following time-dependence $\dot{N}_{\text{ej}}(t) \propto r_{b,\text{bh}}(t)^{-\gamma_{\text{steep},\text{bh}}+\gamma_{\text{rel},\text{bh}}}$, while the orbit-averaged diffusion time dependence remains the same $\mu(\epsilon, t) \propto r_{b,\star}(t)^{-\gamma_{\text{steep},\star}+\gamma_{\text{rel},\star}}$. Hence, the unequal sink term becomes time-dependent for broken-power law distributions.

To compute TDE rates for ultra-steep profiles, we extract the break radius $r_b(t)$ for stars and stellar mass black holes from PhaseFlow (Vasiliev 2017). Then, we compute both the orbit-average diffusion coefficient $\mu(\epsilon, t)$ and the sink term accounting for ejections from strong scatterings (Eq.17- 18). Finally, we integrate the Fokker Planck equation Eq.9 with our time-dependent sink terms.

Fig.5 showcases the evolution of TDE rate enhancements $\dot{N}_\gamma/\dot{N}_{3/2}$ for different ultra-steep profiles where rates are obtained by integrating over a large number of energy bins following Eq.13, with and without strong scattering. Without strong scatterings, TDE rates for

ultra-steep densities of stars and stellar mass black holes are enhanced by up to a factor ~ 200 for $\gamma = 5/2$ and ~ 25 for $\gamma = 9/4$. Those enhancements decrease with time: such as the higher the density slope γ the quicker the decrease. They wash out after a few hundreds Myrs for both profiles and are replaced by small reductions of TDE rates at later times. However when taking into account strong scatterings, enhancements are at most ~ 20 for $\gamma = 5/2$ and ~ 10 for $\gamma = 9/4$. Enhancements only last a few tens Myrs and then *turn into significant reductions for most of the relaxation time*.

5. COMBINATION OF DIFFERENT PRESENT-DAY MASS-FUNCTIONS WITH STELLAR PROPERTIES

A present-day mass function dN/dm_\star (PDMF) of stars is a more realistic representation of an NSC star population than the extensively considered monochromatic distribution. Hence, in sections Sec. 3 and Sec. 4 we considered a Kroupa PDMF (Kroupa 2001).

Simplified PDMFs can be derived from IMFs by setting a cut-off mass to the IMF (Eq.19). Here, the cut-off mass is defined as $m_{\text{max}} = 2M_\odot$ corresponding to a stellar population of age ~ 1.8 Gyr.

Observations have shown that the young stellar population in our galactic center exhibit a top-heavy IMF (e.g., (Bartko et al. 2010; Lu et al. 2013). Moreover, Bortolas (2022) suggested that top-heavy initial IMFs could slightly increase TDE rates. Motivated by this, we explore the effects of combining different PDMFs with either velocity anisotropies or ultra-steep stellar densities.

All IMFs are defined by:

$$\chi(m) \propto \begin{cases} m_\star^{-1.3}, & m_\star < 0.5M_\odot \\ m_\star^{-\alpha}, & m_\star \geq 0.5M_\odot \end{cases} \quad (19)$$

with $\alpha = 2.3$ for Kroupa and $\alpha = \{1.5, 1.7, 1.9\}$ for top-heavy IMFs. Following Magorrian & Tremaine (1999), we also apply a truncation for the smallest masses such as $m_{\text{min}} = 0.08M_\odot$.

In addition to stellar properties, the presence of compact objects also impacts the TDE rates, as their presence enhances the angular momentum diffusion coefficients μ (Eq.2). Throughout this paper, we consider that stars account for 97% of the total mass while stellar mass black holes account for 3% of the total mass and have a mass $m_{\text{bh}} = 15M_\odot$.

Fig.6 showcases the evolution of TDE rates enhancements $\dot{N}_\beta/\dot{N}_{\text{iso}}$ obtained when combining different PDMFs with an anisotropic distribution. The anisotropy factor $\beta_a = 0.5$ is chosen to be the same as in Fig.3 (a value close to the maximum anisotropy factor

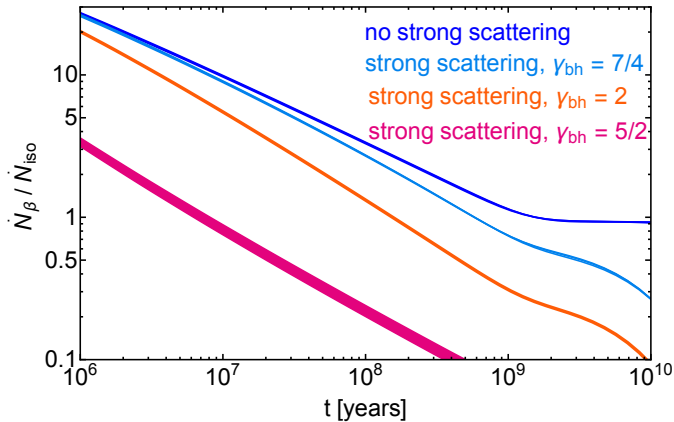


Figure 6. Evolution of TDE Rate enhancements $\dot{N}_\beta / \dot{N}_{\text{iso}}$ for an anisotropy factor $\beta_a = 0.5$ as a function of post-starburst time t . As labeled the different colors correspond to the following different cases: no strong scatterings (blue), strong scatterings with $\gamma_{\text{bh}} = 7/4$ (light blue), strong scatterings with $\gamma_{\text{bh}} = 2$ (orange) and strong scatterings with $\gamma_{\text{bh}} = 5/2$ (pink). The impact of different PDMFs is small and shown in the thickness of the different lines. For all curves, we consider a SMBH mass $M_\bullet = 10^{6.5} M_\odot$ and a density power law of stars $\gamma_\star = 3/2$.

guarantying stability (e.g. Merritt & Aguilar (1985)). The impact of combining different PDMFs with stellar anisotropies is shown in the thickness of the different lines as is minor for all cases. The effect slightly increase when considering strong scatterings and a stellar-mass black hole slope $\gamma_{\text{bh}} = 5/2$. After 10 Myr, enhancements induced by a high anisotropy factor $\beta_a = 0.5$ have completely washed out for a steep profile of stellar mass black holes $\gamma_{\text{bh}} = 5/2$ and are a mere factor 5 – 8 for shallower profiles of stellar mass black holes $\gamma_{\text{bh}} = 7/4 - 2$. TDE rates enhancements when combining different PDMFs with an anisotropic distribution are very similar to enhancements obtained for an anisotropic distribution.

Fig.7 showcases the evolution of TDE rates enhancements $\dot{N}_\gamma / \dot{N}_{3/2}$ when combining different PDMFs with ultra-steep density profiles. As in Fig.6, the impact of combining different PDMFs with stellar anisotropies is shown in the thickness of the different lines and is minor for all cases. We find that combining different PDMFs with ultra-steep density profiles results in a few percents changes in enhancements. Hence, we find that combining different PDMFs with either radial velocity anisotropies or ultra-steep stellar densities cannot explain the post-starburst preference of TDEs when accounting for strong scatterings.

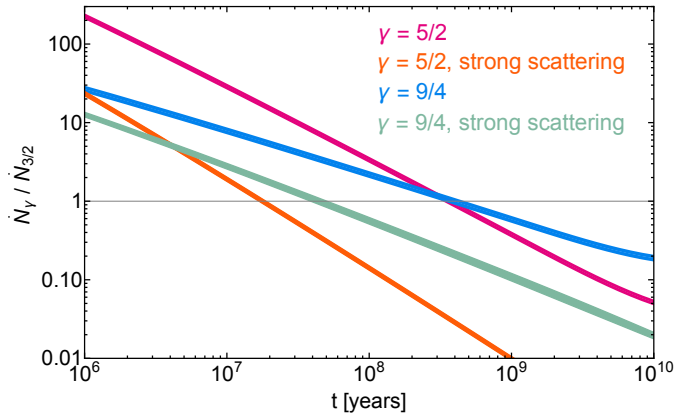


Figure 7. Evolution of TDE Rate enhancements $\dot{N}_\gamma / \dot{N}_{3/2}$ for ultra-steep profiles combined with different PDMFs as a function of post-starburst time t . As labeled the different colors correspond to different initial ultra-steep profiles: $\gamma = 5/2$ without strong scatterings (pink), $\gamma = 5/2$ with strong scatterings (orange), $\gamma = 9/4$ without strong scatterings (blue), $\gamma = 9/4$ with strong scatterings (green). The densities of both stars and stellar mass black holes have been evolved with the code Phaseflow, see Fig. 4. The impact of different PDMFs is small and shown in the thickness of the different lines. For all curves, we consider a SMBH mass $M_\bullet = 10^{6.5} M_\odot$.

6. ALTERNATIVE MODELS FOR TDE ENHANCEMENT RATES

Given our results which challenge the leading suggested scenarios for TDE rate enhancements, it is important to briefly review other suggested scenarios.

6.1. Massive Perturbers and Nuclear Spiral Arms

Before the discovery of the post-starburst preference, Perets et al. (2007b); Perets & Alexander (2008) proposed that massive perturbers, such as giant molecular clouds, could significantly reduce two-body relaxation times and enhance TDE rates. Nuclear spiral arms might have a similar effect (Hamers & Perets 2017). While these mechanisms could preferentially increase TDE rates in gas-rich and post-merger galaxies (which might have preferentially more molecular clouds serving as perturbers), by a small factor, they are unlikely to produce the order of magnitude or more enhancements observed in post-starburst galaxies.

6.2. Binary massive black holes

The first proposed explanation for the post-starburst preference invoked the correlation between starbursts and galaxy mergers (Arcavi et al. 2014). If many post-starburst galaxies are also post-merger galaxies, their nuclei may contain SMBH binaries which can increase TDE rates by many orders of magnitude (relative to galactic nuclei with solitary SMBHs) through a combi-

nation of Kozai cycles (Ivanov et al. 2005) and chaotic three-body scatterings (Chen et al. 2011; Wegg & Bode 2011). However, even though SMBH binaries may temporarily enhance TDE rates by multiple orders of magnitude, the short timescales for such enhancements (typically $\sim 10^5$ yr, e.g. Wegg & Bode 2011) may make it challenging for this mechanism to explain the global fraction of all TDEs seen in post-starburst galaxies (see also discussions in Stone & Metzger 2016; Saxton et al. 2018).

6.3. AGN disk

The influence of an AGN disk on TDE rate has been first explored by (Kennedy et al. 2016) who found enhancements of TDE rates by a factor ~ 10 . Such a factor cannot explain alone the amplitude of observed enhancements. Recently, Wang et al. (2024) explored the "wet" channel for TDEs and found that, enhancements could reach 2 order of magnitude for a very high star formation combined with a high viscosity and a high efficiency (i.e., conversion of the rest mass energy from star formation into radiation). However, such extreme environments require untypical conditions.

6.4. Secular Effects in Eccentric Stellar Disks

Nuclear starbursts can potentially generate eccentric stellar disks where secular effects dramatically increase TDE rates (Madigan et al. 2018; Wernke & Madigan 2019). However, this mechanism requires a relatively small nuclear cluster mass to avoid quenching coherent secular evolution through mass precession. This condition may be problematic for explaining the post-starburst preference, as most low-mass SMBHs coexist with substantial nuclear star clusters. The ideal environment for this mechanism—a disk-dominated nuclear stellar population—is more likely in massive galaxies with SMBHs ($M_\bullet \gtrsim 10^8 M_\odot$), which can only disrupt higher mass of post-main-sequence stars Antonini et al. (2015) and account for a small fraction of observed TDEs (e.g. (Yao et al. 2023))

7. SUMMARY

We studied the scenarios invoking stellar properties to explain the post-starburst preference of TDEs in the

framework of our revised loss cone theory that takes into account both weak and strong scatterings (TSO24). We showed that enhancements induced by radial velocity anisotropies depend both on the anisotropy factor β_a and on the mass of the SMBH: the more massive the SMBH the greater the increase and the longer its duration. When taking into account strong scatterings, we found that radial velocity anisotropies could not explain the post-starburst preference of TDEs except for the rare case of a high mass SMBH $M_\bullet \sim 10^8 M_\odot$ combined with a high radial anisotropy $\beta_a \sim 0.5$ and a shallower profile of stellar-mass black holes $\gamma_{\text{bh}} = 7/4$.

We showed that ultra-steep stellar densities with $\gamma_\star \geq 9/4$ could enhance TDE rates by a factor $\sim 20 - 200$ depending on the density slope, without strong scatterings. However, when taking into account strong scatterings, enhancements induced by ultra-steep stellar densities i) are at most a factor $\sim 10 - 20$ at very early times, ii) *turn into a reduction of TDE rates for most of the relaxation time*. We also found that combining different PDMFs with either ultra-steep stellar densities or radial velocity anisotropies only resulted in very minor changes.

In summary, we have shown that stellar properties that were proposed to explain the post-starburst preference of TDEs, including stellar velocity anisotropies, ultra-steep stellar densities, and the combination of either with top-heavy PDMF *cannot reproduce the observed enhancements, when taking into account both weak and strong scattering*. As we briefly discussed in Section 6 other explanations invoking the influence of a disk or a massive perturber also fail to reproduce either the strength or/and the duration of the enhancements observed (e.g., French et al. (2020)). Hence, our work emphasizes both the importance of taking into account strong scatterings (Teboul et al. 2024) and the need for new hypotheses to explain the post-starburst preference of TDEs.

ACKNOWLEDGEMENTS

We would like to thank Aleksey Genozov for fruitful discussions. OT would like to thank Eugene Vasiliev for his support in the use of Phaseflow.

REFERENCES

- Aharon D., Perets H. B., 2016, ApJL, 830, L1
 Alexander T., Hopman C., 2009, ApJ, 697, 1861
 Amaro-Seoane P., Preto M., 2011, Classical and Quantum Gravity, 28, 094017
 Antonini F., Barausse E., Silk J., 2015, ApJ, 812, 72
 Arcavi I., Gal-Yam A., Sullivan M., Pan Y.-C., Cenko S. B., Horesh A., Ofek E. O., De Cia A., Yan L., Yang C.-W., Howell D. A., Tal D., Kulkarni S. R., Tendulkar S. P., Tang S., Xu D., Sternberg A., Cohen J. G., Bloom J. S., Nugent P. E., Kasliwal M. M., Perley D. A., Quimby R. M., Miller A. A., Theissen C. A., Laher R. R., 2014, ApJ, 793, 38

- Bade N., Komossa S., Dahlem M., 1996, *A&A*, 309, L35
- Bahcall J. N., Wolf R. A., 1976, *ApJ*, 209, 214
- Bahcall J. N., Wolf R. A., 1977, *ApJ*, 216, 883
- Bartko H., Martins F., Trippe S., Fritz T. K., Genzel R., Ott T., Eisenhauer F., Gillessen S., Paumard T., Alexander T., Dodds-Eden K., Gerhard O., Levin Y., Mascetti L., Nayakshin S., Perets H. B., Perrin G., Pfuhl O., Reid M. J., Rouan D., Zilka M., Sternberg A., 2010, *ApJ*, 708, 834
- Bortolas E., 2022, *MNRAS*, 511, 2885
- Broggi L., Bortolas E., Bonetti M., Sesana A., Dotti M., 2022, *MNRAS*, 514, 3270
- Chen X., Sesana A., Madau P., Liu F. K., 2011, *ApJ*, 729, 13
- Cohn H., Kulsrud R. M., 1978, *ApJ*, 226, 1087
- Evans C. R., Kochanek C. S., 1989, *ApJL*, 346, L13
- French K. D., Arcavi I., Zabludoff A., 2016, *ApJL*, 818, L21
- French K. D., Arcavi I., Zabludoff A., 2017, *ApJ*, 835, 176
- French K. D., Wevers T., Law-Smith J., Graur O., Zabludoff A. I., 2020, *SSRv*, 216, 32
- Generozov A., Stone N. C., Metzger B. D., Ostriker J. P., 2018, *MNRAS*, 478, 4030
- Graur O., French K. D., Zahid H. J., Guillochon J., Mandel K. S., Auchettl K., Zabludoff A. I., 2018, *ApJ*, 853, 39
- Hamers A. S., Perets H. B., 2017, *ApJ*, 846, 123
- Hammerstein E., Gezari S., van Velzen S., Cenko S. B., Roth N., Ward C., Frederick S., Hung T., Graham M., Foley R. J., Bellm E. C., Cannella C., Drake A. J., Kupfer T., Laher R. R., Mahabal A. A., Masci F. J., Riddle R., Rojas-Bravo C., Smith R., 2021, *ApJL*, 908, L20
- Hammerstein E., van Velzen S., Gezari S., Cenko S. B., Yao Y., Ward C., Frederick S., Villanueva N., Somalwar J. J., Graham M. J., Kulkarni S. R., Stern D., Bellm E. C., Dekany R., Drake A. J., Groom S. L., Kasliwal M. M., Kool E. C., Masci F. J., Medford M. S., van Roestel J., 2022, arXiv e-prints, p. arXiv:2203.01461
- Hénon M., 1960, *Annales d'Astrophysique*, 23, 668
- Hills J. G., 1975, *Nature*, 254, 295
- Holoien T. W. S., Kochanek C. S., Prieto J. L., Stanek K. Z., Dong S., Shappee B. J., Grupe D., Brown J. S., Basu U., Beacom J. F., Bersier D., Brimacombe J., Danilet A. B., Falco E., Guo Z., Jose J., Herczeg G. J., Long F., Pojmanski G., Simonian G. V., Szczygiel D. M., Thompson T. A., Thorstensen J. R., Wagner R. M., Woźniak P. R., 2016, *MNRAS*, 455, 2918
- Ivanov P. B., Polnarev A. G., Saha P., 2005, *MNRAS*, 358, 1361
- Kaur K., Stone N. C., 2024, arXiv e-prints, p. arXiv:2405.18500
- Kennedy G. F., Meiron Y., Shukirgaliyev B., Panamarev T., Berczik P., Just A., Spurzem R., 2016, *MNRAS*, 460, 240
- Kroupa P., 2001, *MNRAS*, 322, 231
- Lacy J. H., Townes C. H., Hollenbach D. J., 1982, *ApJ*, 262, 120
- Law-Smith J., Ramirez-Ruiz E., Ellison S. L., Foley R. J., 2017, *ApJ*, 850, 22
- Lezhnin K., Vasiliev E., 2015, *ApJL*, 808, L5
- Lu J. R., Do T., Ghez A. M., Morris M. R., Yelda S., Matthews K., 2013, *ApJ*, 764, 155
- Madigan A.-M., Halle A., Moody M., McCourt M., Nixon C., Wernke H., 2018, *ApJ*, 853, 141
- Magorrian J., Tremaine S., 1999, *MNRAS*, 309, 447
- Masterson M., De K., Panagiotou C., Kara E., Arcavi I., Eilers A.-C., Frostig D., Gezari S., Grotova I., Liu Z., Malyali A., Meisner A. M., Merloni A., Newsome M., Rau A., Simcoe R. A., van Velzen S., 2024, *ApJ*, 961, 211
- Merritt D., 2013, *Dynamics and Evolution of Galactic Nuclei*
- Merritt D., Aguilar L. A., 1985, *MNRAS*, 217, 787
- Perets H. B., Alexander T., 2008, *ApJ*, 677, 146
- Perets H. B., Hopman C., Alexander T., 2007a, *ApJ*, 656, 709
- Perets H. B., Hopman C., Alexander T., 2007b, *ApJ*, 656, 709
- Preto M., Amaro-Seoane P., 2010, *ApJL*, 708, L42
- Rees M. J., 1988, *Nature*, 333, 523
- Saxton C. J., Perets H. B., Baskin A., 2018, *MNRAS*, 474, 3307
- Stone N. C., Generozov A., Vasiliev E., Metzger B. D., 2018, *MNRAS*, 480, 5060
- Stone N. C., Metzger B. D., 2016, *MNRAS*, 455, 859
- Teboul O., Stone N. C., Ostriker J. P., 2024, *MNRAS*, 527, 3094
- TSO24 O., 24, *MNRAS*, 527, 3094
- van Velzen S., 2018, *ApJ*, 852, 72
- Vasiliev E., 2017, *ApJ*, 848, 10
- Wang J., Merritt D., 2004, *ApJ*, 600, 149
- Wang M., Ma Y., Wu Q., Jiang N., 2024, *ApJ*, 960, 69
- Wegg C., Bode J., 2011, *ApJL*, 738, L8
- Wernke H. N., Madigan A.-M., 2019, *ApJ*, 880, 42
- Yao Y., Ravi V., Gezari S., van Velzen S., Lu W., Schulze S., Somalwar J. J., Kulkarni S. R., Hammerstein E., Nicholl M., Graham M. J., Perley D. A., Cenko S. B., Stein R., Ricarte A., Chadayammuri U., Quataert E., Bellm E. C., Bloom J. S., Dekany R., Drake A. J., Groom S. L., Mahabal A. A., Prince T. A., Riddle R., Rusholme B., Sharma Y., Sollerman J., Yan L., 2023, *ApJL*, 955, L6
- Young P., 1980, *ApJ*, 242, 1232
- Zhang F., Amaro Seoane P., 2024, *ApJ*, 961, 232

APPENDIX

A. LOCAL DIFFUSION COEFFICIENT

The local diffusion coefficient we evaluate in Eq. 2 is given by (Magorrian & Tremaine 1999; Wang & Merritt 2004):

$$\lim_{R \rightarrow 0} \frac{\langle (\Delta R)^2 \rangle}{2R} = \frac{32\pi^2 r^2 G^2 \langle m_\star^2 \rangle \ln \Lambda}{3J_c^2(\epsilon)} (3I_{1/2}(\epsilon) - I_{3/2}(\epsilon) + 2I_0(\epsilon)) \quad (\text{A1})$$

with:

$$I_0(\epsilon) \equiv \int_0^\epsilon f(\epsilon') d\epsilon \quad (\text{A2})$$

and

$$I_{n/2}(\epsilon) \equiv [2(\psi(r) - \epsilon)]^{-n/2} \int_\epsilon^{\psi(r)} [2(\psi(r) - \epsilon')]^{n/2} f(\epsilon') d\epsilon'. \quad (\text{A3})$$

B. ORBIT AVERAGED EJECTION RATES

Here we present the the orbit averaged ejection rate for which we derived a simple analytical closed forms in Teboul et al. (2024).

For an equal mass scatterer and $\gamma_\star = 3/2$, we obtained:

$$\langle \dot{N}_{\text{ej}} \rangle = \frac{2^{1/2} \pi \rho_{\text{infl}} m G^{1/2} r_{\text{infl}}^{3/2} (4 - 3(1 - e^2)^{1/2})}{(\gamma_\star + 1) M^{3/2} (1 - e^2)^{1/2}}. \quad (\text{B4})$$

For an equal mass scatterer, with $\gamma_\star = 5/2$, we obtained:

$$\langle \dot{N}_{\text{ej}} \rangle = \frac{2^{-1/2} \pi \rho_0 m G^{1/2} r_0^{5/2} (-4 + 12e^2 + 5(1 - e^2)^{3/2})}{(\gamma_\star + 1) M^{3/2} a (1 - e^2)^{3/2}}. \quad (\text{B5})$$

C. ANALYTICAL SOLUTIONS TO THE FOKKER-PLANCK EQUATION WITH STRONG SCATTERINGS

In (Teboul et al. 2024), we derived analytical solutions for the modified Fokker-Planck equation Eq.9 using the method of Frobenius. A comparison between our analytical solutions and numerical solutions can be found in (Teboul et al. 2024) (Fig.4 for equal mass scatterers, Fig.5 for unequal mass scatterers).

C.1. Equal mass scatterer

For equal mass scatterers, the analytical solutions for $\gamma_\star = 3/2$ and $\gamma_\star = 5/2$ write:

$$\begin{aligned} f_{3/2}(j) &= (1 + 16Aj)(a + b \ln j) - 32Abj \\ f_{5/2}(j) &= e^{\frac{-4\sqrt{2A}}{\sqrt{j}}} j^{1/4} [ag_-(j) + be^{\frac{8\sqrt{2A}}{\sqrt{j}}} g_+(j)] \end{aligned} \quad (\text{C6})$$

with $g_\pm = 1 \pm \frac{\sqrt{j}}{32\sqrt{2A}} + 0.0022 \frac{j}{A}$ and two undetermined constants $-b$ and a - need to be found. $A = \langle \dot{N}_{\text{ej}} \rangle / \mu(\epsilon)$ is the sink term whose analytical formula can be found in Appendix B.

Their explicit time-dependence comes from the undetermined constants a and b . In practice, b is deterministically set as a function of a using the absorbing boundary condition at $j = j_o$, so there is only one true time-dependent free parameter. We find that a depends on the dimensionless time τ as $a \sim \tau^{-1/2}$.

C.1.1. *Unequal mass scatterer*

We derived analytical solutions to the modified Fokker-Planck equation Eq.9 for the following stellar-mass black holes slopes: $\gamma_{\text{bh}} = 3/2, 7/4, 2, 9/4$ and $5/2$. The resulting closed form solutions write:

$$\begin{aligned}
f_{3/2,u}(j) &= (1 + 4Aj)(a + b \ln j) - 8Ajb \\
f_{7/4,u}(j) &= (1 + 8A\sqrt{j})^2 \left(a - \frac{b}{2}(2 \ln 16A + \ln j) \right) \\
&\quad - 2b(\gamma_E + 16A(-1 + \gamma_E)\sqrt{j} + 32A^2(-3 + 2\gamma_E)j) \\
f_{2,u}(j) &= j^{-2\sqrt{A}}(j^{4\sqrt{A}}a + b) \\
f_{9/4,u} &= e^{-8\sqrt{A}j^{-1/4}} j^{1/8} \left(\frac{\sqrt{\pi b}}{2A^{1/4}} \left(-1 + \frac{j^{1/4}}{64A^{1/2}} \right) \right. \\
&\quad \left. + \frac{a}{2\sqrt{2\pi}} \cosh(8\sqrt{A}j^{-1/4}) \right) \\
f_{5/2,u}(j) &= e^{\frac{-4\sqrt{A}}{\sqrt{j}}} j^{1/4} [ah_-(j) + be^{\frac{8\sqrt{A}}{\sqrt{j}}} h_-(j)]
\end{aligned} \tag{C7}$$

where γ_E is Euler's constant and $h_{\pm} = 1 \pm \frac{\sqrt{j}}{32\sqrt{A}} + 0.0044 \frac{j}{A}$.